

PACS numbers: 42.65.Jx; 42.60.Jf; 52.38.Hb; 52.50.Jm
DOI: 10.1070/QE2013v043n01ABEH015007

Filamentation of IR and UV femtosecond pulses upon focusing in air

A.A. Dergachev, A.A. Ionin, V.P. Kandidov, L.V. Seleznev, D.V. Sinitsyn, E.S. Sunchugasheva, S.A. Shlenov

Abstract. **The filamentation of IR and UV laser pulses has been studied numerically and experimentally for different initial beam focusing geometries, and linear electron density profiles along the plasma channel of filaments have been obtained. The results demonstrate that changes in laser beam focusing have a stronger effect on filament and plasma channel parameters for UV radiation than for IR radiation. Focusing causes individual high fluence regions produced by refocusing to merge to form a continuous extended filament with a continuous plasma channel.**

Keywords: *filamentation, femtosecond laser pulse, laser-induced plasma, UV filaments.*

1. Introduction

The propagation of high-power femtosecond laser radiation is accompanied by self-trapping of the beam and the formation of thin extended filaments [1–4]. The high intensity of the optical field in the filaments leads to photoionisation of the medium, and the laser pulse produces plasma channels with a relatively high free electron concentration.

In the initial stage of filamentation, the laser beam undergoes self-focusing due to the Kerr nonlinearity of the medium. The process takes place when the peak laser output power exceeds the critical power for self-focusing in the medium, P_{cr}, which decreases significantly with decreasing laser wavelength. The critical power for self-focusing in air is 2–6 GW at a wavelength of 800 nm and about 70 MW at 248 nm. Because of this, UV filaments can be obtained using considerably lower laser pulse energies.

The self-trapping of laser light and the forming plasma channels determine the application area of filamentation [5, 6]. As pointed out in a number of reports, UV filaments have significant advantages in several applications, e.g. in the creation of atmospheric waveguides [7, 8], LIBS [9], remote sensing of explosives [10] and microhole drilling [11]. Ionin et al. [12] considered the use of UV pulses for controlling an electric discharge. According to their results, a combination of a train of picosecond UV pulses and a long UV pulse increases the discharge photocurrent by two orders of magnitude relative to the current due to a single long pulse.

As pointed out in the first reports [13, 14], the UV generation of a laser plasma occurs at a considerably lower multiphoton ionisation order than does the IR generation. Whereas the photoionisation of oxygen and nitrogen molecules at a wavelength of 800 nm requires 8 and 11 photons, respectively, that at 248 nm requires just three and four photons. As a result, the balance between the Kerr self-focusing and the plasma-induced defocusing of light in UV filaments is more delicate than that in IR filaments. Tzortzakis et al. [13] point out that this leads to a greater length of UV filaments in comparison with IR filaments. According to experiments with tightly focused beams [15] and numerical simulations for collimated beams [16], the plasma channel diameter in UV filaments is smaller than that in IR filaments. As shown in studies of UV filamentation [17], the plasma channel diameter and electron concentration increase with pulse duration. In a theoretical study, Schwarz and Diels [18] assumed the possibility of producing UV filaments several hundred millijoules in energy and several kilometres in length.

Numerical simulations of UV filamentation were performed for near-laboratory conditions and beams focused by a lens with a focal length of several metres. The characteristics of UV and IR filaments were examined independently. According to Fedorov and Kandidov [16], in the case of collimated light the peak intensity and fluence are weak functions of wavelength, whereas the electron concentration in the plasma channel decreases with increasing wavelength. As shown by Geints and Zemlyanov [19], the transverse size of the maximum intensity region of a focused femtosecond laser beam at 800 nm depends on beam parameters and varies insignificantly across the self-trapping region. Papazoglou et al. [20] found a relationship between structural changes in fused silica and plasma channels in filaments and evaluated the electron concentration at which permanent structural changes in fused silica are caused by even a single laser pulse.

In this paper, we examine the filamentation of focused light at wavelengths of 800 and 248 nm in a wide range of focal lengths. To compare the UV and IR filamentation effects, we consider pulses at identical parameters determining the initial stage of filamentation.

2. Model and numerical experiment

In numerical simulation of the propagation of a femtosecond laser pulse in air, we used a self-consistent system of equations for a slowly varying complex amplitude of an optical field,

A.A. Dergachev, V.P. Kandidov, S.A. Shlenov Department of Physics, M.V. Lomonosov Moscow State University, Vorob'evy gory, 119991 Moscow, Russia; International Laser Center, M.V. Lomonosov Moscow State University, Vorob'evy gory 1, 119991 Moscow, Russia; e-mail: dergachev88@yandex.ru, kandidov@phys.msu.ru, shlenov@phys.msu.ru;
A.A. Ionin, L.V. Seleznev, D.V. Sinitsyn, E.S. Sunchugasheva P.N. Lebedev Physics Institute, Russian Academy of Sciences, Leninsky prosp. 53, 119991 Moscow, Russia

Received 25 September 2012; revision received 16 October 2012
Kvantovaya Elektronika **43** (1) 29–36 (2013)
Translated by O.M. Tsarev

$A(r,z,\tau)$, and the free electron concentration, $n_e(r,z,\tau)$. In the axisymmetric approximation, this system, written using the 'retarded' time $\tau = t - zn_0/c$, has the form

$$2ik_0\frac{\partial A}{\partial z} = \frac{1}{r}\frac{\partial}{\partial r}\left(r\frac{\partial A}{\partial r}\right) + \tilde{D}A + \frac{2k_0^2}{n_0}(\Delta n_K + \Delta n_{pl})A - ik_0\delta A, \quad (1)$$

$$\Delta n_K(r,z,\tau) = \frac{1}{2}n_2 I(r,z,\tau) + \frac{1}{2}\int_{-\infty}^{\tau} n_2 I(r,z,t')H(t-t')\mathrm{d}t', \quad (2)$$

$$\Delta n_{pl}(r,z,\tau) = -\frac{\omega_{pl}^2(r,z,\tau)}{2n_0\omega_0^2}, \quad \omega_{pl}^2(r,z,\tau) = \frac{4\pi e^2}{m_e}n_e(r,z,\tau),$$
$$n_e = n_e^{(1)} + n_e^{(2)}, \quad (3)$$

$$\frac{\partial n_e^{(1,2)}}{\partial \tau} = R^{(1,2)}(I)(n_0^{(1,2)} - n_e^{(1,2)}). \quad (4)$$

Here, $k_0 = 2\pi/\lambda$ is the wavenumber; n_0 is the refractive index of the undisturbed medium at the centre wavelength of the pulse; Δn_K and Δn_{pl} are the changes in the refractive index of air due to the Kerr and plasma nonlinearities, respectively; I is the radiation intensity; $n_e^{(1)}$ and $n_e^{(2)}$ are the electron concentrations due to the ionisation of oxygen and nitrogen molecules in air, respectively; $n_0^{(1)}$ and $n_0^{(2)}$ are the initial concentrations of oxygen and nitrogen molecules; e is the electron charge; and m_e is the electron mass. The first term in the equation for the complex field amplitude describes diffraction in the parabolic approximation. The dispersion in the medium, denoted by an operator $\tilde{D}$, was taken into consideration in a spectral representation, so that

$$A(z+\Delta z) = FFT^{-1}\{FFT[A(z)]\exp(ik_0 n(\omega)\Delta z)\}. \quad (5)$$

For the refractive index, we used the Cauchy formula,

$$n(\lambda) = 1 + A(1 + B/\lambda^2), \quad (6)$$

with $A = 2.879\times10^{-4}$ and $B = 5.67\times10^{-11}$ cm^2 [21].

In evaluating the Kerr nonlinearity contribution, both the instantaneous and delayed responses were taken into account [22]. The convolution kernel in (2) has the form

$$H(t) = \Omega^2\exp\left(-\frac{\Gamma t}{2}\right)\frac{\sin \Lambda t}{\Lambda}, \quad (7)$$

where $\Omega = 20.6$ THz; $\Gamma = 26$ THz; and $\Lambda = \sqrt{\Omega^2 - \Gamma^2/4}$ [23]. The cubic nonlinearity coefficient is $n_2 = 4\times10^{-19}$ cm^2 W^{-1} at a wavelength of 800 nm and 13.4×10^{-19} cm^2 W^{-1} at 248 nm [24–26], which corresponds to a critical power for self-focusing of 2.4 GW and 70 MW, respectively. The plasma nonlinearity is determined by the free electron concentration, n_e. In our calculations, a two-component model of air was used, with $n_0^{(1)}$ and $n_0^{(2)}$ initial concentrations of 21% and 79% of the total concentration of molecules in air: $n_M = 2.7\times10^{19}$ cm^{-3}.

The ionisation rates of oxygen and nitrogen molecules, $R^{(1,2)}$, in (4) were determined by the optical field intensity I. The $R^{(1,2)}$ rates at a wavelength of 800 nm were evaluated in the PPT model [27]. In the UV region, the multiphoton approximation is applicable at any intensity:

$$R(I) = \sigma I^K, \quad (8)$$

where $K = [1 + W/\hbar\omega_0]$ is the minimum number of photons of centre frequency ω_0 whose total energy exceeds the ionisation potential of the molecule, W, and σ is the photoionisation cross section. We took $K^{(1)} = 3$ and $\sigma^{(1)} = 1.34\times10^{-27}$ cm^6 s^{-1} W^{-3} for oxygen and $K^{(2)} = 4$ and $\sigma^{(2)} = 2.4\times10^{-43}$ cm^8 s^{-1} W^{-4} for nitrogen [14, 17, 28]. Figure 1 shows the photoionisation rate as a function of incident intensity at wavelengths of 800 and 248 nm.

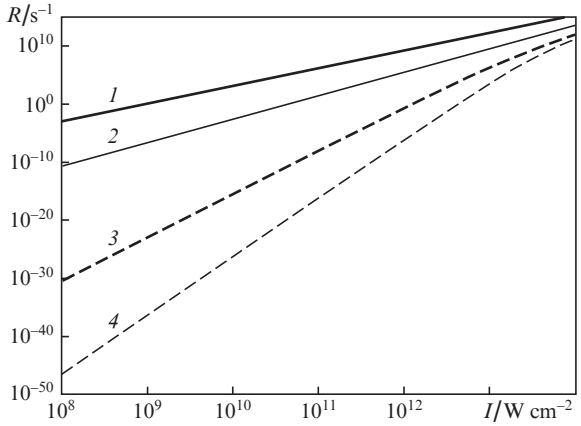

Figure 1. Ionisation rates of (*1*, *3*) oxygen and (*2*, *4*) nitrogen as functions of laser intensity at wavelengths of (*1*, *2*) 248 and (*3*, *4*) 800 nm.

The coefficient δ in (1) is related to the energy loss through the photoionisation of the medium by

$$\delta = \frac{1}{I}\left(K^{(1)}\hbar\omega_0\frac{\partial n_e^{(1)}}{\partial t} + K^{(2)}\hbar\omega_0\frac{\partial n_e^{(2)}}{\partial t}\right). \quad (9)$$

The complex amplitude of the optical field was taken in the form

$$A(r, z=0, \tau) = A_0\exp\left(-\frac{r^2}{2r_0^2}\right)\exp\left(\mathrm{i}\frac{k_0 r^2}{2f}\right)\exp\left(-\frac{\tau^2}{2\tau_0^2}\right), \quad (10)$$

where r_0 is the beam radius; τ_0 is the 1/e pulse width; and f is the radius of curvature of the phase front.

In numerically solving the problem, we used the split-step method. At each integration step, linear and nonlinear factors were taken into account separately. The diffraction operator was approximated using an implicit difference scheme. To accurately represent the dispersion of the medium, we used a spectral-domain solution.

Even for an axisymmetric system, the problem of filamentation (1)–(4) requires considerable computational resources. This is caused by the necessity of high spatial and temporal resolutions of the difference mesh, which is in turn related to the distinctive features of the solution, namely, to the small structures forming in the beam and pulse. Another difficulty is presented by the calculation of focused beams: first, because of the large initial beam size and, second, because of the larger beam divergence behind the linear focus in comparison with collimated beams. Typical spatial and temporal mesh resolutions in our computations were 1 μm and 0.5 fs, and the total number of nodes in the computational mesh was up to 3400 along the spatial coordinate and 2048 along the time coordinate. To solve the problem in question, we used parallel programming methods and resources of the Chebyshev and

Lomonosov supercomputers (Research Computing Center, M.V. Lomonosov Moscow State University) [29].

The simulation results were used to evaluate the following filament and plasma channel parameters: fluence,

$$F(r,z) = \int_{-\infty}^{\infty} I(r,z,\tau)d\tau \text{ (J cm}^{-2}\text{)};$$

peak axial intensity,

$$I_{\max}(z) = \max_{\tau} I(r=0,z,\tau) \text{ (W cm}^{-2}\text{)};$$

plasma density in the wake of a pulse,

$$N_e(r,z) = n_e(r,z,\tau=\infty) \text{ (cm}^{-3}\text{)};$$

linear plasma density,

$$\rho_{\text{lin}}(z) = \int_0^{\infty} N_e(r,z)2\pi r\,dr \text{ (cm}^{-1}\text{)};$$

total number of free electrons,

$$Q_e^{\text{tot}} = \iint_0^{\infty} N_e(r,z)2\pi r\,dr\,dz;$$

filament (r_{fil}) and plasma channel (r_{pl}) radii (cm) (determined at the 1/e fluence (F) or electron concentration (N_e) level; and the integral filament radius,

$$r_{\text{integr}}(z) = \left[\int F(r,z)r^2 2\pi r\,dr\left(\int F(r,z)2\pi r\,dr\right)^{-1}\right]^{1/2} \text{ (cm)}.$$

The value of r_{integr} was determined by integrating over a circle with $r < 0.85$ mm in order to obtain the average over the self-trapping region of the filament.

The initial laser pulse parameters are listed in Table 1. To compare IR and UV filamentation, we considered 248- and 800-nm radiations at identical pulse durations (τ_0), beam radii (r_0) and focal lengths (f). In addition, the peak laser output power, P, was taken such that the ratio of P to the critical power for self-focusing, P_{cr}, which determines the initial stage of filamentation, was the same at the two wavelengths. In our numerical simulations, we used $P/P_{\text{cr}} = 10$, which ensured the formation of a single filament in the beam cross section. The other similarity parameters of the problem were then different: diffraction length, $l_{\text{dif}} = k_0 r_0^2$; dispersion length, $l_{\text{disp}} = \tau_0^2/k''_\omega$; and the distance to the filament start, z_{fil}, evaluated from numerical simulation results. Comparison of the above parameters indicates that the higher dispersion and greater diffraction length in the UV spectral region compared to the IR lead to delay of filament formation at a given difference between the peak power and critical power. In particular, at a focal length $f = 50$ m (so-called weak focusing) the distance to the filament start is 35 m in the UV and 19 m in the IR. It is worth noting that, in the absence of focusing, UV pulse propagation is accompanied by no filamentation because of the severe dispersion-induced broadening.

3. Numerical simulation results

Figures 2 and 3 present numerical modelling results for the filamentation of IR and UV pulses, respectively. It is seen that, in the case of weak focusing for IR and UV pulses, the filament breaks up into a sequence of regions with a high fluence, $F(r,z)$, and high electron concentration, $N_e(r,z)$, due to refocusing [3]. At the beam parameters under consideration, the extent of an individual region is about 50 cm and the regions are 2–3 m apart. In the case of tight focusing ($f = 5$ m), individual high fluence regions merge to form a continuous filament owing to the energy inflow from the periphery of the beam. The fluence in the filament, $F(r,z)$, then increases by only a factor of 2–4, and its length decreases to 1–1.5 m. In the case of weak focusing, the high fluence regions in the filament and the plasma channel are located before the linear focus of the system, whereas in the case of tight focusing the filament extends 10–20 cm beyond the geometric focus. Note that this distance agrees with the length of the linear beam waist (12 and 40 cm for the UV and IR pulses, respectively), where pulse refocusing is possible.

The influence of beam focusing on the filamentation behaviour of the beam can be qualitatively interpreted in terms of the moving-focus model for femtosecond radiation [3]. In the case of weak focusing, like in a collimated beam geometry, energy localisation in an extended filament is caused by the self-focusing of temporal slices of the pulse at its centre and leading edge. If the pulse power is sufficiently high, subsequent energy localisation is caused, among other things, by refocusing: radiation defocused in a laser-induced plasma can be focused owing to Kerr nonlinearity [30]. Refocusing covers temporal slices of the trailing part of the pulse, where no nonlinear focus was formed and only defocusing in the plasma induced by the preceding temporal slices took place. Refocusing occurs as well in those temporal slices where a nonlinear focus was formed and then defocusing occurred in the laser-induced plasma of the preceding temporal slices.

Hypothetically, in a quasi-steady state representation, a filament in a collimated beam should be infinitely long if there is no absorption. In focused radiation in the absence of refocusing, a filament should extend to the end of the waist because it corresponds to infinity for a collimated beam. An attempt to eliminate the inconsistency between physical ideas and experimental and theoretical results was made by Geints and Zemlyanov [31], who evaluated the filament length using the Bouguer formula with nonlinear absorption caused by the loss through photoionisation of the medium.

That femtosecond filaments have a finite length is due to the transient nature of the spatiotemporal energy localisation process. Indeed, for the temporal slices that are separated from the leading edge of the pulse by an interval approaching

Table 1. Laser pulse parameters used in numerical simulation.

λ/nm	τ_0/fs	r_0/mm	f/m	E/mJ	P/P_{cr}	$I_{\max}$/W cm^{-2}	l_{dif}/m	l_{disp}/m	z_{fil}/m
800	60	4	50/5	2.5	10	4.6×10^{10}	125	132	19/4.2
248	60	4	50/5	0.07	10	1.3×10^{9}	405	41	35/4.7

Note: λ is the centre wavelength; τ_0, r_0 and f are the pulse duration, beam radius and radius of curvature of the phase front in (10); E is the pulse energy; P is the peak pulse power (we give the ratio to the critical power for self-focusing, P_{cr}, at the specified wavelength); $I_{\max}$ is the initial peak pulse intensity; l_{dif} is the diffraction length; l_{disp} is the dispersion length of the pulse; and z_{fil} is the distance to the filament start (for two focal lengths).

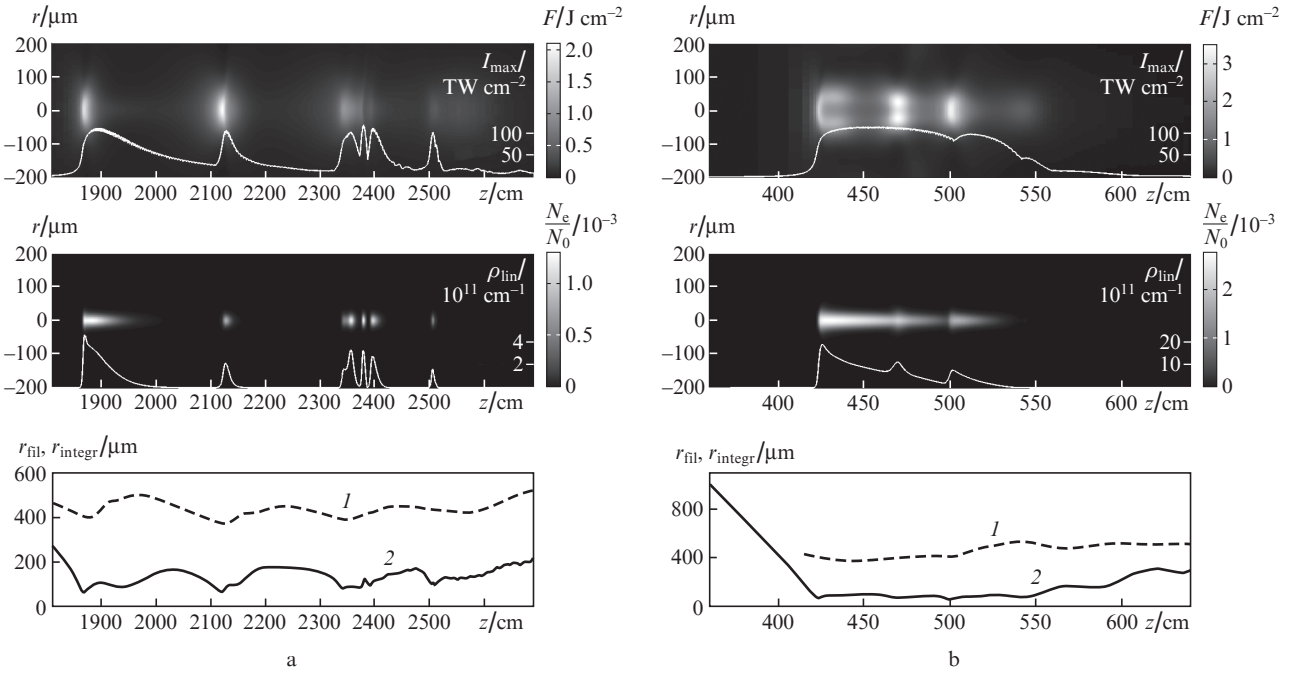

Figure 2. Fluence profiles $F(r,z)$ (upper panels), plasma density profiles $N_e(r,z)$ (middle panels) and (*1*) r_{fil} and (*2*) r_{integr} filament radii (lower panels) for IR pulse filamentation in the case of (a) weak and (b) tight beam focusing. The solid lines in the upper panels represent the peak axial pulse intensity I_{max} as a function of propagation distance along the z axis. In the middle panels, the solid lines show the linear plasma density ρ_{lin} as a function of z.

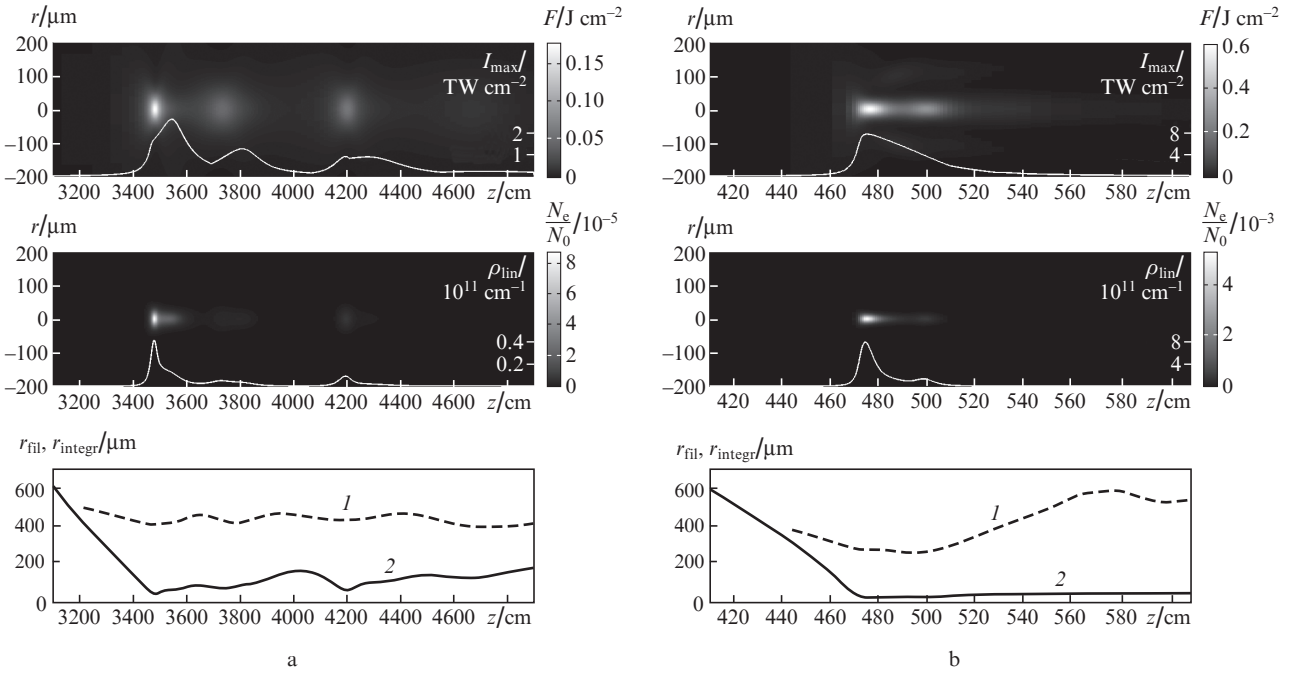

Figure 3. Same as in Fig. 2, but for a UV pulse.

the delay time of the Kerr response, the critical power for self-focusing increases, and the increase is larger for shorter intervals. Moreover, reducing the power in the temporal slices at the leading edge reduces the duration of the intensity peak that results from the spatial beam compression under self-focusing conditions. This increases the dispersion-induced broadening of the forming intensity peak, which limits the self-focusing-induced increase in intensity and can suppress the formation of a nonlinear focus in the temporal slices where the power exceeded the critical power for self-focusing. As shown earlier [32, 33], a high group velocity dispersion in the absence of plasma generation and energy losses can prevent beam collapse and, hence, radiation filamentation. In particular, under the present simulation conditions the dispersion

Table 2. Parameters of filaments and plasma channels of IR and UV pulses for weak and tight focusing.

λ/nm	f/m	r_{fil}/μm	r_{pl}/μm	I_{max}/TW cm^{-2}	F_{max}/J cm^{-2}	N_e^{max}/N_0	ρ_{lin}/cm^{-1}	Q_e^{tot}
800	50	80–150	20–40	25–120	0.5–2	1.2×10^{-3}	7×10^{11}	4.6×10^{13}
	5	100	20–30	100–120	1–3.5	2.3×10^{-3}	2×10^{12}	8×10^{13}
248	50	45–100	20–30	0.25–2.6	0.03–0.2	1×10^{-4}	4×10^{10}	4.6×10^{12}
	5	25–50	13–30	8	0.2–0.6	5×10^{-3}	8×10^{11}	9.5×10^{12}

Note. The filament (r_{fil}) and plasma channel (r_{pl}) radii were determined at the e^{-1} fluence (F) and plasma density (N_e) levels, respectively.

length decreases by more than a factor of 100 because of the pulse self-compression in a filament and, according to our estimates, is at least 1 m in the IR and 0.3 m in the UV. Dispersion-induced broadening has a stronger effect on the filamentation of UV radiation. According to numerical simulation results, no UV filamentation occurs in collimated radiation with the parameters given in Table 1, but an IR filament does form.

Linear losses, as well as losses due to ionisation during self-focusing, may arrest beam collapse. According to numerical simulation results, the loss due to the generation of all the plasma in a filament is 4% and 7% for weak and tight focusing of IR radiation, respectively, and 20% and 40% for UV radiation. The high relative loss due to ionisation for UV radiation can be accounted for as follows: The total number of free electrons in the plasma, Q_e^{tot} (Table 2), and the absolute energy loss due to the ionisation in a UV filament are about one order of magnitude smaller than those in an IR filament. At the same time, at a given P/P_{cr} ratio and pulse duration the UV pulse energy is 35 times lower than the IR pulse energy.

As a result, before refocusing occurs the peak axial pulse intensity and electron concentration decrease significantly along the filament, and the high fluence and laser-induced plasma regions become shorter. A filament of collimated femtosecond radiation is then finite even when there are no linear losses in the medium. In a focused beam, the radiation converges to the beam axis, maintaining energy localisation on the filament axis to the end of the waist. Subsequent refocusing leads to the formation of a high fluence/electron concentration region beyond the waist of the focused beam. A filament beyond the focus of a lens was first detected by Lange et al. [34].

Graphs of the filament radius r_{fil} versus distance can be used to determine the cross-sectional size of the energy localisation region. Before filament formation, r_{fil} is large and coincides with the beam radius. In a filament, r_{fil} drops to 25–100 μm, depending on beam parameters. The low $r_{fil}(z)$ value obtained numerically beyond the filamentation region is the consequence of the locality of this parameter, which becomes inapplicable to a beam profile severely distorted after filamentation. Figures 2 and 3 present the integral radius r_{integr} in the filamentation region. It considerably exceeds the r_{fil} at the 1/e level because the filament is surrounded by a large energy reservoir. The increase in $r_{integr}(z)$ beyond the filament reflects the global radiation divergence beyond the waist of the focused beam. Such divergence is particularly large in the case of tight focusing [35].

Note that, because of the high energy flux to the propagation axis due to tight focusing, one of the refocusings in an IR pulse has the form of a ring (Fig. 2b, upper panel, $z = 470$ cm). Moreover, as a result of tight focusing the rings resulting from the interference of the convergent light with the optical field defocused by a self-induced laser plasma [36] remain localised near the beam propagation axis (Fig. 2b, upper panel, $z =$ 440 cm; Fig. 3b, upper panel, $z = 480-520$ cm).

Quantitative characteristics of filaments and plasma channels are presented in Table 2. For parameters that vary widely along a filament or plasma channel, we indicate their spread. It is seen in the first two lines that reducing the distance to the linear focus by ten times causes no significant changes in any parameters of the IR filament or its plasma channel. The r_{fil} and r_{pl} radii and maximum intensity in the filament change very little, whereas the maximum fluence and the linear and bulk plasma densities increase by a factor of 2–3. It can be stated with certainty that, in the focusing range examined, the IR filament and plasma channel parameters are determined not so much by geometric focusing as by nonlinear refraction.

At the same time, in the case of a UV pulse a similar change in focusing leads to significant changes in filament and plasma channel parameters. The radii of the structures decrease by a factor of two, and the maximum intensity in the filament increases by three times. The linear and bulk plasma densities increase by one and half orders of magnitude. Thus, during UV pulse filamentation the linear focusing effect has a considerably stronger influence on the energetic and geometric parameters of the filaments and plasma channels.

The difference in the relationship between linear and nonlinear factors for IR and UV pulses is caused by the difference between the multiphoton ionisation orders at the wavelengths under consideration. Whereas, according to (8), the ionisation rate of oxygen molecules, $R^{(1)}$, at 248 nm is proportional to I^3, at 800 nm we have $R^{(1)} \propto I^8$ at intensities below 10^{12} W cm^{-2}. At higher intensities, the deviation of the process from multiphoton ionisation becomes significant, and $R^{(1)}$ decreases somewhat. For the ionisation rate of nitrogen, we have $R^{(2)} \propto I^4$ at 248 nm and $R^{(2)} \propto I^{11}$ at 800 nm. The power law behaviour of the plasma nonlinearity as a function of intensity has a large exponent. As a consequence, the electron concentration increases sharply with increasing intensity along the filament. The plasma-induced phase shift varies strongly with time and over the cross section of the filament, considerably exceeding the geometric/optical phase gradient. For UV radiation, the electron concentration is a significantly weaker function of intensity. As a consequence, the gradient of the plasma-induced nonlinear phase shift is lower. The geometric/optical focusing of UV radiation can have a stronger effect on filament formation and parameters. The difference in ionisation rate between IR and UV radiations has a marked effect on filament parameters in the case of weak focusing, where the nonlinearity contribution is more significant.

In the case of UV radiation, the photoionisation of the medium begins at lower laser field intensities, leading to earlier defocusing and, as a consequence, to mild filament formation. Because of this, the highest axial intensity is reached behind the high fluence region (Fig. 3a), where the focused pulsed radiation peak diminishes, as does the electron concentration in the laser-induced plasma, responsible for defocusing. As a

result, a balance between the Kerr and plasma nonlinearities in the UV filament is reached at a peak intensity (I_{max}), peak electron concentration (N_e^{max}), fluence (F_{max}) and linear plasma density (ρ_{lin}) one to two orders of magnitude lower than those for IR radiation. Therefore, UV filamentation is closer to a guided propagation mode than is IR filamentation.

4. Experimental

Figure 4 shows a schematic of the experimental setup. The 744-nm radiation from a Ti:sapphire laser and its third harmonic (248 nm) were used to study IR and UV filamentation. Convergent beams of 4 mm radius with focal lengths of 110 and 100 cm at wavelengths of 744 and 248 nm, respectively, were formed by spherical mirrors. The pulse duration (FWHM) was 100 fs. The linear plasma density ρ_{lin} was measured using a capacitor in the form of two 1-cm-radius hemispheres whose centres lay on a normal to the plasma channel being measured. The gap between the hemispheres was 2–3 mm. The formation of a plasma channel in a filament between the hemispheres changed the capacitance of the capacitor, and the recharge current was measured with an oscilloscope. Since the change in the capacitance depended on the electron concentration and the length and width of the plasma channel between the spheres, the measured recharge current was proportional to the linear plasma density in the filament.

Figure 5 shows the measured linear plasma density profiles along a filament formed near the waist by 744- and 248-nm

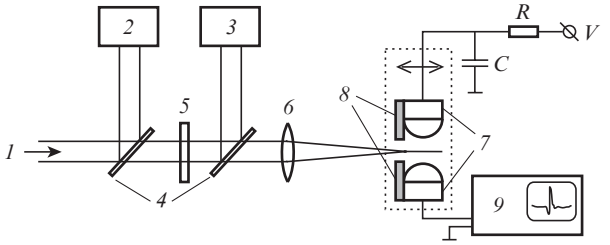

Figure 4. Schematic of the experimental setup: (*1*) laser radiation, (*2*) autocorrelator, (*3*) energy meter, (*4*) beam splitters, (*5*) attenuator, (*6*) lens, (*7*) electrodes, (*8*) aperture, (*9*) oscilloscope. The voltage applied to the electrodes is $V = 300$ V.

radiations at two pulse energies. These results demonstrate that, with increasing IR or UV pulse energy, the length of the plasma channel increases and its front end shifts closer to the incident light. The electron concentration in the plasma channel of the IR radiation sharply drops behind the geometric focus, whereas in the case of the UV radiation it extends beyond the focus of the beam. The linear plasma density profile $\rho_{lin}(z)$ obtained by numerically solving the system of Eqns (1)–(4) with the radiation parameters used in our experiments agrees with the present experimental data. The two maxima in the linear-density profile obtained numerically for the plasma of the IR filament seem to be responsible for the

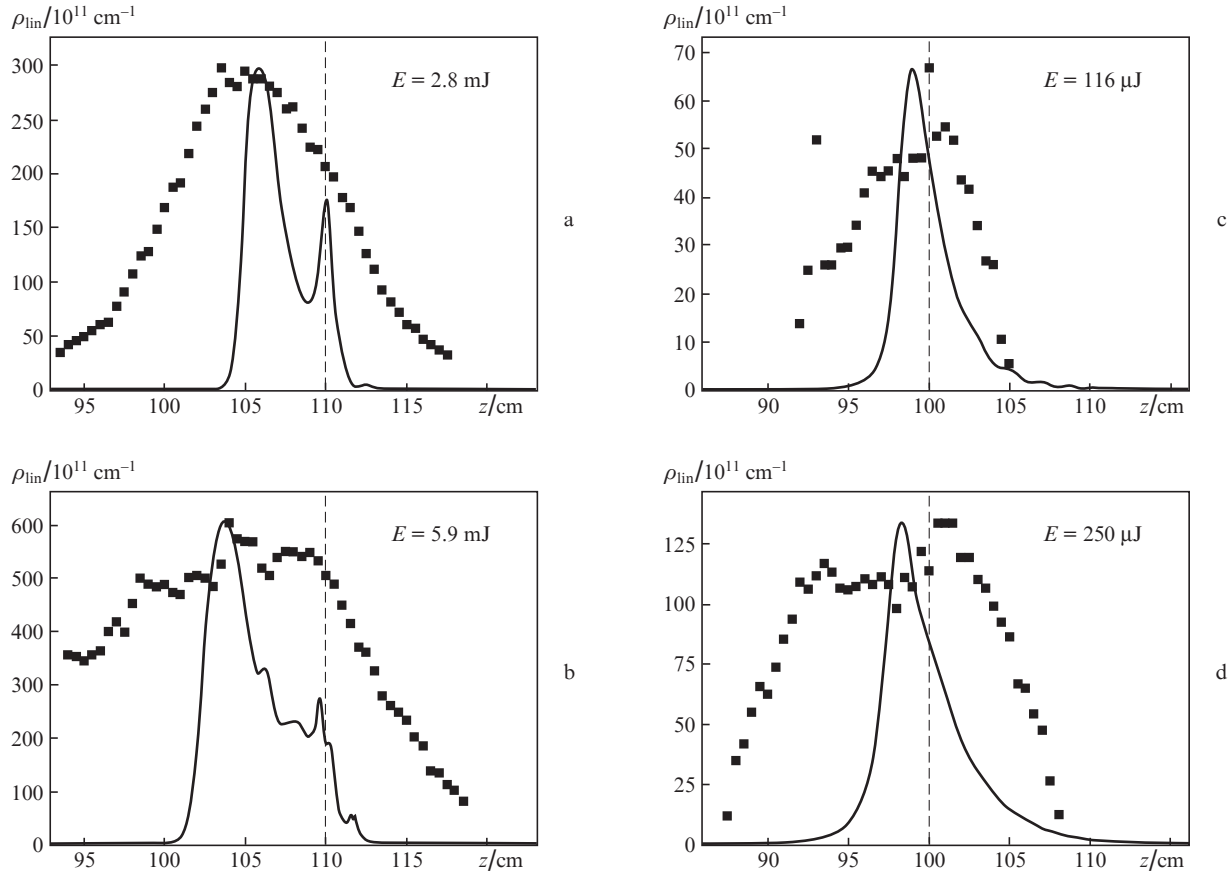

Figure 5. Linear plasma density (ρ_{lin}) profiles along the pulse propagation direction. For 744-nm pulses (a, b), the distance to the geometric focus of the system was 110 cm; for 248-nm pulses (c, d), the distance was 100 cm (the focal plane is represented by the dashed line). The solid squares represent the experimental data and the solid lines represent the simulation results at different initial pulse energies, E.

local extrema in experimental $\rho_{\text{lin}}(z)$ data. One maximum corresponds to the filament start point, and the other coincides with the geometric focus of the beam. The profile for the UV pulse has only one maximum, near the geometric focus, and the plasma channel persists behind the focal plane.

The differences between the measured and simulated plasma channel lengths can be related to the finite aperture of the measuring capacitor. The spatial resolution is determined by the dimensions of the region whose conductivity has a significant effect on the capacitance of the capacitor. For the hemispheres used, such a region may be several centimetres in size, and the measurands are effectively averaged within it. This may account as well for the fact that the measured profile in the plasma channel of the IR radiation has only one peak.

5. Conclusions

The filamentation of IR and UV femtosecond laser pulses in air at a peak power ten times the critical power has been studied numerically and experimentally for different beam focusing geometries. The results indicate that tight focusing can lead to the coalescence of individual regions of high fluence and high plasma density that result from multiple refocusing, whereas in the case of weak focusing such regions are separated in the pulse propagation direction. According to Matvienko et al. [37], tight focusing leads to 'continuous' filamentation, and weak focusing, to 'discontinuous' filamentation.

The absolute filament length in the case of tight focusing is shorter than that in the case of weak focusing. In the case of tight focusing, the filament may extend beyond the linear focus of the system owing to refocusing over a distance comparable to the initial beam waist length. Because of the large energy inflow from the periphery of the beam to the propagation axis, the rings of the radiation defocused by the self-induced laser plasma remain localized near the optical axis of the beam.

The differences in quantitative parameters between filaments and plasma channels of IR and UV pulses arise mainly from the different dependences of the photoionisation rate of gaseous species in air on laser radiation intensity. High photoionisation rates for UV radiation lead to earlier termination of the self-focusing process in the case of weak focusing, which results in a lower laser field intensity in the filament and a lower free electron concentration in the plasma channel. The lower multiphoton ionisation order in the case of UV radiation leads to a stronger effect of geometric focusing on filament formation and facilitates control over filament parameters. At a sufficiently tight focusing, the free electron concentration in the plasma channel of a UV pulse is comparable to parameters of the plasma channel of an IR pulse. The present numerical simulation results are consistent with our measurements for tightly focused 744- and 248-nm radiations.

Acknowledgements. This work was supported by the Russian Foundation for Basic Research (Grant Nos 11-02-12061, 10-02-01477, 11-02-01100 and 11-02-90421-Ukr_f_a) and the Educational–Scientific Complex, P.N. Lebedev Physics Institute, Russian Academy of Sciences (scholarship programme). A.A. Dergachev, V.P. Kandidov and S.A. Shlenov acknowledge the support from the RF Ministry of Education and Science (Grant Nos NSh-6897.2012.2 and 8393).

References

1. Chin S.L., Hosseini S.A., Liu W., Luo Q., Théberge F., Aközbek N., et al. *Can. J. Phys.*, **83**, 863 (2005).
2. Couairon A., Mysyrowicz A. *Phys. Rep.*, **441**, 47 (2007).
3. Kandidov V.P., Shlenov S.A., Kosareva O.G. *Kvantovaya Elektron.*, **39**, 205 (2009) [*Quantum Electron.*, **39**, 205 (2009)].
4. Chin S.L. *Femtosecond Laser Filamentation* (New York: Springer, 2010, p. 130).
5. Kasparian J., Wolf J.-P. *Opt. Express*, **16**, 466 (2008).
6. Xu H.L., Chin S.L. *Sensors*, **11**, 32 (2011).
7. Schwarz J., Rambo P., Giuggioli L., Diels J.-C. *Proc. OSA/NLGW*, **WC6**, 467 (2001).
8. Schwarz J., Diels J.-C. *Proc. SPIE Int. Soc. Opt. Eng.*, **4632**, 122 (2002).
9. Tzortzakis S., Anglos D., Gray D. *Opt. Lett.*, **31**, 1139 (2006).
10. Mirell D., Chalus O., Peterson K., Diels J.-C. *J. Opt. Soc. Am. B*, **25**, B108 (2008).
11. Schwarz J., Diels J.-C. *Appl. Phys. A*, **77**, 185 (2003).
12. Ionin A.A., Kudryashov S.I., Levchenko A.O., Seleznev L.V., Shutov A.V., et al. *Appl. Phys. Lett.*, **100**, 104105 (2012).
13. Tzortzakis S., Lamouroux B., Chiron A., Franco M., Prade B., Mysyrowicz A. *Opt. Lett.*, **25**, 1270 (2000).
14. Schwarz J., Rambo P., Diels J.-C., Kolesik M., Wright E.M., Moloney J.V. *Opt. Commun.*, **180**, 383 (2000).
15. Bukin O.A., Bykova E.E., Geints Yu.E., Golik S.S., Zemlyanov A.A., Il'in A.A., Kabanov A.M., Matvienko G.G., Oshlakov V.K., Sokolova E.B. *Opt. Atmos. Okeana*, **24**, 351 (2011) [*Atmos. Oceanic Opt.*, **24**, 351 (2011)].
16. Fedorov V.Yu., Kandidov V.P. *Laser Phys.*, **12**, 1530 (2008).
17. Tzortzakis S., Lamouroux B., Chiron A., et. al. *Opt. Commun.*, **197**, 131 (2001).
18. Schwarz J., Diels J.-C. *J. Mod. Opt.*, **49**, 2583 (2002).
19. Geints Yu.E., Zemlyanov A.A. *Opt. Atmos. Okeana*, **23**, 274 (2010) [*Atmos. Oceanic Opt.*, **23**, 274 (2010)].
20. Papazoglou D.G., Zergioti I., Tzortzakis S. *Opt. Lett.*, **32**, 2055 (2007).
21. Born M., Wolf E. *Principles of Optics* (Oxford: Pergamon, 1969; Moscow: Nauka, 1970).
22. Oleinikov P.A., Platonenko V.T. *Laser Phys.*, **3**, 618 (1993).
23. Mlejnek M., Wright E.M., Moloney J.V. *Opt. Lett.*, **23**, 382 (1998).
24. Loriot V., Hertz E., Faucher O., Lavorel B. *Opt. Express*, **17**, 13429 (2009).
25. Nibbering E.T.J., Grillon G., Franco M.A., Prade B.S., Mysyrowicz A. *J. Opt. Soc. B*, **14**, 650 (1997).
26. Shaw M.J., Hooker C.J., Wilson D.C. *Opt. Commun.*, **103**, 153 (1993).
27. Perelomov A.M., Popov V.S., Terent'ev M.V. *Zh. Eksp. Teor. Fiz.*, **50**, 1393 (1966).
28. Couairon A., Tzortzakis S., Bergé L., Franco M., Prade B., Mysyrowicz A. *J. Opt. Soc. Am. B*, **19**, 1117 (2002).
29. Dergachev A.A., Silaeva E.P., Shlenov S.A. *Superkomp'yuternye tekhnologii v nauke, obrazovanii i promyshlennosti* (Supercomputer Technologies in Science, Education and Industry) (Moscow: Mosk. Univ., 2010) p. 100.
30. Kandidov V.P., Kosareva O.G., Broder A., Chin S.L. *Opt. Atmos. Okeana*, **10**, 1539 (1997) [*Atmos. Oceanic Opt.*, **10**, 966 (1997)].
31. Geints Yu.E., Zemlyanov A.A. *Opt. Atmos. Okeana*, **24**, 641 (2011) [*Atmos. Oceanic Opt.*, **24**, 641 (2011)].
32. Zharova N.A., Litvak A.G., Petrova T.A., Sergeev A.M., Yunakovskii A.L. *Pis'ma Zh. Eksp. Teor. Fiz.*, **44**, 12 (1986).
33. Luther G.G., Newell A.C., Moloney J.V. *Phys. D*, **74**, 59 (1994).
34. Lange H.R., Grillon G., Ripoche J.-F., Franco M.A., Lamouroux B., Prade B.S., Mysyrowicz A., Nibbering E.T.J., Chiron A. *Opt. Lett.*, **23**, 120 (1998).

35. Geints Yu.E., Zemlyanov A.A., Kabanov A.M., Matvienko G.G., Stepanov A.N. *Opt. Atmos. Okeana*, **22**, 119 (2009) [*Atmos. Oceanic Opt.*, **22**, 119 (2009)].
36. Chin S.L., Petit S., Liu W., Iwasaki A., Nadeau M.-C., Kandidov V.P., Kosareva O.G., Andrianov K.Yu. *Opt. Commun.*, **210**, 329 (2002).
37. Matvienko G.G., Geints Yu.E., Zemlyanov A.A., Kabanov A.M. *Materialy XVIII Mezhdunarodnogo simpoziuma 'Optika atmosfery i okeana. Fizika atmosfery'* (Proc. XVIII Int. Symp. on Atmospheric and Oceanic Optics and Atmospheric Physics) (Irkutsk, 2012) p. 8.